





# Quantitative multiphoton imaging of cell metabolism, stromal fibers, and keratinization enables label-free discrimination of esophageal squamous cell carcinoma

FENG XIANG,<sup>1,2,†</sup>  JIA YU,<sup>1,2,3,†</sup> DANLING JIANG,<sup>4</sup> WEIWANG HU,<sup>1,2</sup> RONGLI ZHANG,<sup>1,2</sup>  CHENMING HUANG,<sup>1,2</sup> TING WU,<sup>1,2</sup> YUFENG GAO,<sup>1,2</sup> AIPING ZHENG,<sup>5</sup> TZU-MING LIU,<sup>3</sup> WEI ZHENG,<sup>1,2,6</sup> XI LI,<sup>4,7</sup> AND HUI LI<sup>1,2,8</sup>

<sup>1</sup>Research Center for Biomedical Optics and Molecular Imaging, Shenzhen Key Laboratory for Molecular Imaging, Guangdong Provincial Key Laboratory of Biomedical Optical Imaging Technology, Shenzhen Institute of Advanced Technology, Chinese Academy of Sciences, Shenzhen 518055, China

<sup>2</sup>CAS Key Laboratory of Health Informatics, Shenzhen Institute of Advanced Technology, Chinese Academy of Sciences, Shenzhen 518055, China

<sup>3</sup>Institute of Translational Medicine, Faculty of Health Sciences & Ministry of Education Frontiers Science Center for Precision Oncology, University of Macau, Taipa, Macau, China

<sup>4</sup>Department of Gastroenterology, Peking University Shenzhen Hospital, Shen Zhen 518036, China

<sup>5</sup>Department of Pathology, Peking University Shenzhen Hospital, Shen Zhen 518036, China

<sup>6</sup>zhengwei@siat.ac.cn

<sup>7</sup>lixil22188@sina.com

<sup>8</sup>hui.li@siat.ac.cn

<sup>†</sup>These authors contributed equally to this work.

**Abstract:** Esophageal squamous cell carcinoma (ESCC) features atypical clinical manifestations and a low 5-year survival rate (< 5% in many developing countries where most of the disease occurs). Precise ESCC detection and grading toward timely and effective intervention are therefore crucial. In this study, we propose a multidimensional, slicing-free, and label-free histopathological evaluation method based on multispectral multiphoton fluorescence lifetime imaging microscopy (MM-FLIM) for precise ESCC identification. To assess the feasibility of this method, comparative imaging on fresh human biopsy specimens of different ESCC grades is performed. By constructing fluorescence spectrum- and lifetime-coded images, ESCC-induced morphological variations are unveiled. Further quantification of cell metabolism and stromal fibers reveals potential indicators for ESCC detection and grading. The specific identification of keratin pearls provides additional support for the early detection of ESCC. These findings demonstrate the viability of using MM-FLIM and the series of derived indicators for histopathological evaluation of ESCC. As there is an increasing interest in developing multiphoton endoscopes and multiphoton FLIM systems for clinical use, the proposed method would probably allow noninvasive, label-free, and multidimensional histological detection and grading of ESCC in the future.

© 2023 Optica Publishing Group under the terms of the [Optica Open Access Publishing Agreement](#)

## 1. Introduction

Esophageal cancer is the seventh most frequent cancer and the sixth leading cause of cancer deaths worldwide, with approximately 604,000 new cases and 544,000 deaths in 2020 [1]. Esophageal squamous cell carcinoma (ESCC) is the predominant histological type of esophageal cancer, accounting for ~84% of all cases [2]. The 5-year survival rate of ESCC is less than 5% in many developing countries where most of the disease occurs, as the majority of patients are diagnosed

with advanced cancer at initial diagnosis due to the atypical clinical manifestations [3]. As such, precise detection and grading toward timely and effective intervention of ESCC are crucial.

Over the past few decades, Lugol's chromoendoscopy has been extensively used in the clinical diagnosis of ESCC, as it allows dysplastic or malignant changes to be highlighted using Lugol's iodine [3,4]. However, the staining may cause irritant esophagitis, hypersensitivity reactions, aspiration pneumonia, or other complications [5–8]. As an alternative, several optical enhancement techniques, such as flexible spectral imaging color enhancement (FICE), magnifying endoscopy with narrow-band imaging (ME-NBI), and blue laser imaging (BLI), have been recently reported for effective detection of ESCC [9,10]. However, limited by the low spatial resolution (macroscopic or mesoscopic scale), an invasive biopsy followed by histopathological examination is still inevitable for diagnosis of ESCC. The histopathological examination is not only limited to *ex vivo* assessment and two-dimensional morphology characterization, but also suffers from complicated and time-consuming sample processing that involves paraffin microtomy, staining, and so on. Owing to the sub-cellular resolution, the emerging confocal laser endomicroscopy enables noninvasive and real-time histological diagnosis *in vivo* [11,12]; however, similar to chromoendoscopy, exogenous contrast agents, such as fluorescein sodium and acriflavine hydrochloride, are still necessary [11,13,14]. These fluorescent dyes often carry the risk of side effects (e.g. acriflavine, which binds to nucleic acids, is potentially mutagenic), and none of them are FDA approved for endoscopic imaging [15]. Overall, a multi-dimensional, high-resolution, label-free, and noninvasive method is of considerable interest for histopathological evaluation of ESCC.

Multiphoton microscopy (MPM) can achieve histological imaging with sub-cellular resolution, relying on two-photon excitation fluorescence (TPEF) and second harmonic generation (SHG) of intrinsic molecules [16–19]. Owing to the near-infrared and localized excitation, MPM has several advantages benefitting *in vivo* applications over confocal laser microscopy, including deep tissue penetration, reduced photobleaching and photodamage, and intrinsic optical sectioning ability [20–22]. Recently, a multispectral fluorescence lifetime detection technique was integrated into MPM, offering further quantitative insights into the biochemical properties of living tissues, such as structural composition, cell metabolism, and local environmental variations [23–25]. With the superiority in morphological and functional imaging, the combined technology (namely multispectral multiphoton fluorescence lifetime imaging microscopy [MM-FLIM]) shows tremendous potential for multidimensional, noninvasive, and label-free histopathological examination. To date, MM-FLIM has been reported to detect various digestive tract cancers, such as oral, gastric, and colorectal carcinomas, based on endogenous reduced nicotinamide adenine dinucleotide (NADH), flavin adenine dinucleotide (FAD), collagen, bilirubin, keratin, or tryptophan *in vitro* or *in vivo* [24,26–30]. Unfortunately, esophageal cancer remains a virtually untapped area of the MM-FLIM application field that has yet to be explored.

In this study, we systematically imaged the most prevalent esophageal cancer, ESCC, using MM-FLIM relying solely on intrinsic signals. To mimic clinical settings, en face imaging of fresh human specimens was performed. The derived fluorescence spectrum- and lifetime-coded images revealed three-dimensional (3D) structural variations in esophageal mucosa during ESCC progression. Further quantification of cell metabolism and stromal fibers based on the MM-FLIM images then provided potential indicators of ESCC detection and grading. Additionally, the keratin pearl, which is a histopathological marker of well and moderately differentiated ESCC [31,32], could be easily distinguished from other tissue components according to the fluorescence spectrum and lifetime. Synergizing this point with the other indicators proposed above would allow precise discrimination and even early detection of ESCC. These results demonstrate the viability of using MM-FLIM to discern ESCC of different grades by assessing cell metabolism, stromal fibers, and keratinization. Coupled with the advancement of clinical-available multiphoton endoscopes [33][34] and multiphoton FLIM systems [35–37], MM-FLIM appears to hold promise

for noninvasive, label-free, and multidimensional histopathological evaluation of ESCC in the future.

## 2. Materials and methods

### 2.1. Patients and sample preparation

Fresh human esophageal mucosal specimens were collected from 11 patients of Peking University Shenzhen Hospital (Shenzhen, China) by gastroscopy or surgical resection. The 11 patients included four with mucosa inflammation, five with MD cancer, and two with PD cancer. Normal specimens were collected from the tissue adjacent to lesions in patients with inflammation. Patients with cancer provided T specimens, while PT tissues (> 5 cm away from the tumor margin) were also collected in some cases for paired comparison (Table S1, [Supplement 1](#)). Standard histopathological examination was conducted in all cases on half of each specimen for clinical diagnosis by professional pathologists. The remaining half was immediately imaged using MM-FLIM within 3 h, and no special sample processing was performed except for soaking it in phosphate-buffered saline (PBS; pH 7.4) to avoid dehydration and shrinkage. Because long-term sample storage and special sample processing will likely influence the environment and optical characteristics of endogenous fluorophores. To facilitate imaging, the wet specimen was sandwiched between a glass slide and a coverslip. The surface of the esophageal mucosa was kept against the coverslip to face the objective lens and mimic gastroscopy-view imaging. To prevent tissue deformation, the edge of the coverslip was supported by a backup ring around the tissue on the glass slide. For each specimen, one to five imaging sites were randomly selected. All of the experimental procedures were approved by the Ethics Committee for Human Research, Peking University Shenzhen Hospital (Ethics Approval No. 2022037), and prior informed consent was obtained from all participants.

### 2.2. Imaging instrumentation

In this study, we used a home-built MM-FLIM system to perform quantitative and label-free MPM imaging on esophageal mucosae. The system has been described in detail in our previous work [38]. In brief, a mode-locked femtosecond Ti:sapphire laser (Chameleon Ultra, Coherent, California, USA) was used as the excitation source by tuning to 750 nm. Two-dimensional images ( $350\ \mu\text{m} \times 350\ \mu\text{m}$ ) were created at a pixel dimension of  $256 \times 256$  via raster scanning the laser beam using a couple of galvanometer mirrors (TSH8310, Sunny Technology, Beijing, China). Following scanning, the laser beam was passed through a scan lens, a tube lens, and a dichroic mirror (FF685-Di02, Semrock, New York, USA), before being focused onto the sample by a water immersion objective (XLUMPLFLN, 20 $\times$ , NA 1.0, Olympus, Tokyo, Japan). The excited MPM signals were collected using the same objective and split from the excitation laser by the dichroic mirror above. The residual excitation light was removed with a 680-nm short-pass filter (FF01-680/SP-25, Semrock, New York, USA) and the MPM signals were conducted on a spectrograph via a fiber bundle for spectral recording. The detector of the spectrograph was a 16-channel linear-array photomultiplier tube (PMT, PML-16-C, Becker & Hickl GmbH, Berlin, Germany). The 16 channels covered a spectral range of 350–550 nm, with an interval of 12.5 nm. Finally, a time-correlated single photon counting module (TCSPC, SPC-150, Becker & Hickl GmbH, Berlin, Germany) was connected to the detector to record the fluorescence decay curve of each spectral band into 256 time channels. The full width at half maximum of the system's instrument response function was  $\sim 220$  ps, which was measured by recording the reflected femtosecond laser pulses. Using the system, fluorescence spectrum- and lifetime-resolved images of fresh human esophageal mucosal specimens were acquired at a rate of 16 s/frame. For volumetric imaging, the objective was axially translated using a motorized actuator (KMMS25E/M, Thorlabs, Newton, New Jersey, USA) with a step size of 3  $\mu\text{m}$ . The

laser power on the sample was controlled  $<10$  mW during superficial imaging and gradually increased with the increase of imaging depth to overcome excitation light attenuation caused by tissue absorption and scattering. There was no obvious photodamage or photobleaching observed during imaging.

### 2.3. Mucosal component segmentation

Limited by the imaging depth of label-free MPM, only the superficial esophageal mucosa was investigated in this study, and the structural components that could be observed mainly included cells and collagen fibers. In addition, elastin fibers and keratin pearls were found in some specimens. To investigate the characteristics and differences of these four structural components, it was necessary to separate them from each other. The MPM signal is composed of SHG signals (350–400 nm, spectral channels 1–4), which primarily originate from collagen, and TPEF signals (400–550 nm, spectral channels 5–16) from cells (mitochondrial NADH), elastin, and keratin pearls. In practice, it is straightforward to segment collagen fibers from the image by separating the SHG signals from the TPEF signals according to the emission spectra (Fig. S1, the magenta part, [Supplement 1](#)), while an image segmentation algorithm based on the arithmetic of different spectral channels was used for other components with mixed TPEF signals (Fig. S1 and Fig.S2, [Supplement 1](#)). For ease of description, the spectral channel has been shortened to “Ch” hereafter. Please also note that the center wavelength and wavelength band of each spectral channel presented in this study was theoretically calculated according to spectral detection range (350–550 nm) and spectral channel interval (12.5 nm) of our imaging system. The numbers are used just to facilitate method description, and the significant digits didn't indicate the spectral resolution. The actual spectral resolution of the system is  $\sim 12.5$  nm.

In this study, the observed elastin fibers can be generally divided into two cases according to their distribution characteristics. One is being scattered in the interspace between irregular cell clusters, in which case we manually separated the elastin fibers from the TPEF image for subsequent analysis, while the other is being concentrated around the tumor nest and mixing with collagen fibers, with a clear observable boundary between the fibers and cells. In the latter case, an elastin mask was created as follows (Fig. S1, the cyan part, [Supplement 1](#)). First, the SHG mask and TPEF mask were obtained on the basis of the SHG image and TPEF image, respectively, using an operation named mask generation (MG). The operation involves three steps: creating a binary mask using a threshold  $Th$ ; filling holes with area  $< H_{\text{area}}$ ; and removing small objects occupying area  $< O_{\text{area}}$ . The values of  $Th$ ,  $H_{\text{area}}$ , and  $O_{\text{area}}$  are given beside the step in Fig. S1, [Supplement 1](#) [39]. Second, the inverted SHG mask and the TPEF mask were logically joined using the AND operation; then, the third MG step was performed to generate the cell mask. Finally, by inverting the cell mask, the elastin mask was obtained.

Keratin pearls are composed of concentric rings of squamous cells showing gradual keratinization and are usually present within abnormal cell clusters [40]. As there is a red shift in the spectral peak of keratin relative to NADH [41], the keratin pearl was primarily separated from surrounding cells by subtracting Ch 5–8 (400–450 nm, mainly NADH) from Ch 10–16 (462.5–550 nm, mainly keratin). Then, the MG operation was performed on the raw keratin pearl image, and the resulting mask was logically joined with the cell mask using the AND operation. Subsequently, by further performing the third MG step, the mask of the keratin pearl was obtained (Fig. S1, the golden part, [Supplement 1](#)). The mask of abnormal cells was accordingly generated via subtracting the keratin mask from the cell mask.

All of the arithmetic and manual operations on images were performed using ImageJ (National Institutes of Health, Bethesda, Maryland, USA) and the other steps were performed using custom MATLAB (Math Works, Natick, Massachusetts, USA) programs. The obtained MM-FLIM images as well as the segmentation results of the various structural components presented in normal and cancerous esophageal mucosae were carefully discussed by the authors with

professional pathologists and confirmed by the gold standard hematoxylin and eosin (H&E) stained histopathological images.

#### 2.4. Fluorescence spectrum analysis

To reveal the general spectral characteristics of normal and cancerous esophageal mucosae, spectrum-coded images were created using custom MATLAB programs according to the following steps. First, each spectral channel was assigned a certain RGB color. Second, a color-coded intensity image of each spectral channel was created by multiplying the assigned RGB color values with the intensity image of corresponding spectral channel pixel by pixel. Third, the 16 color-coded intensity images added up to a spectrum-coded image. Obviously, each pixel in the spectrum-coded image is a weighted summation of the 16 color-coded spectral channels that uses the emission intensity of each channel as the weight, and thus its color can generally reflect the emission peak. Note that for each spectral channel, signals in the 256 time channels were integrated for all the spectral analysis. Additionally, the spectrum was obtained via integrating the signals of one  $z$ -section at each spectral channel. For structural-component-resolved analysis, only signals in the area of the component were integrated. From the TPEF spectrum, the TPEF spectral ratio (the ratio of TPEF signals with long wavelength [Ch10,  $468.75 \pm 6.25$  nm] over those with short wavelength [Ch7,  $431.25 \pm 6.25$  nm]) was derived to quantitatively characterize the spectral shifts among different groups. Another spectral parameter, SHG/TPEF (the ratio of signals from the channel with maximum SHG [Ch3,  $381.25 \pm 6.25$  nm] over those from the channel with maximum TPEF [Ch8,  $443.75 \pm 6.25$  nm; Ch9,  $456.25 \pm 6.25$  nm; or Ch10,  $468.75 \pm 6.25$  nm]) was calculated to characterize the relative content of collagen fibers.

#### 2.5. Fluorescence lifetime analysis

The fluorescence decay process in biological samples generally resembles a linear combination of multiple single exponential decays, each corresponding to a specific fluorophore. NADH was the primary origin of cellular autofluorescence in our study, as 750 nm excitation wavelength was used [42], and it exists in two forms in tissue: free and protein-bound [43]. Therefore, we chose the following bi-exponential function model for fluorescence lifetime analysis:

$$f(t) = \alpha_1 e^{-\frac{t}{\tau_1}} + \alpha_2 e^{-\frac{t}{\tau_2}}, \quad (1)$$

where  $\tau_1$  and  $\tau_2$  represent the lifetimes of the two fluorophore components, and  $\alpha_1$  and  $\alpha_2$  represent the relative fractions of the two components. To calculate fluorescence lifetime parameters, the model was first convolved with the instrument response function of the system, and then fitted to the obtained fluorescence decay curves. Afterwards, the mean fluorescence lifetime can be obtained as follows:

$$\tau_{\text{mean}} = \frac{\alpha_1 \tau_1 + \alpha_2 \tau_2}{\alpha_1 + \alpha_2}. \quad (2)$$

For fair comparison with NADH, bi-exponential fitting was also used for acellular structures, and  $\tau_{\text{mean}}$  was eventually used for comparison. Fluorescence lifetime-coded images were created by color coding  $\tau_{\text{mean}}$  for each pixel. Here, signals from all spectral channels were integrated to form the fluorescence decay curve of each pixel in the calculation. In terms of quantitative comparison, TPEF signals (Ch 5–16, 400–550 nm) within a given mucosal component in one  $z$ -section were integrated to form a single decay curve to calculate  $\tau_{\text{mean}}$ , while, particularly for collagen fibers, SHG signals (Ch 1–4, 350–400 nm) were integrated. Then,  $\alpha_1/\alpha_2$  was further calculated to quantify the ratio of the short-lifetime fluorophore component to the component with a relative long lifetime in the cell metabolism assessment. The fluorescence lifetime-coded images were generated using SPCImage software (Becker & Hickl), while other calculations were conducted with MATLAB programming.



## 2.6. Statistical analysis

Comparisons of three or more groups were performed using one-way analysis of variance followed by the Tukey's multiple comparison test.  $P$ -values  $< 0.05$  were considered statistically significant. All of the error bars presented in this study denote the standard error of the mean (SEM), which takes into account both the value of the standard deviation and the sample size. All the statistics, including tests of significance and error analysis, as well as all the graphing of quantitative results were performed with GraphPad Prism 7 (GraphPad software, San Diego, California, USA) and following the guideline of the software. The amount of data in each group is shown in Table S1, [Supplement 1](#). Note that for statistically quantifying the fluorescence spectral and lifetime characteristics of cellular autofluorescence, cells in a  $z$  section were segmented as a whole, and the signals within the segmented area were integrated to obtain a single fluorescence spectral curve or fluorescence decay curve with acceptable signal-to-noise ratio. The same went for other structural components, and only one data point was derived from the  $z$  stack of an imaging site by averaging the data of the  $z$  sections. For paired comparison of PT and T sites, the presented statistics were obtained via further averaging PT and T data points derived from a single patient, respectively, and no error bars were provided due to the small sample size

## 3. Results

### 3.1. MM-FLIM images reveal structural variations in esophageal mucosa during ESCC progression

To evaluate the potential of MM-FLIM for multidimensional, slicing-free, and label-free histopathological examination of ESCC, we performed systematic MM-FLIM imaging on esophageal mucosae with ESCC of different grades, including normal, moderately differentiated (MD) carcinoma, and poorly differentiated (PD) carcinoma. To mimic clinical settings, fresh human biopsy specimens were collected and en face imaging relying solely on intrinsic signals was performed.

Histologically, the shallow esophageal mucosa consists mainly of an epithelial lining formed by stratified squamous epithelium and a lamina propria of loose fibroelastic connective tissue. The connective tissue invaginates the epithelium as papillae, and is separated from the epithelium by a thin basement membrane [44]. By constructing 3D fluorescence spectrum- (Fig. 1(A)–(C)) and lifetime-coded images (Fig. 1(D)–(F)), we captured dramatic mucosal changes induced by the occurrence and progression of ESCC. Specifically, typical stratified squamous epithelium, which mainly consists of superficial prickly cells (white arrows in Fig. 1(A), (D)) and deep-seated basal cells (yellow arrows in Fig. 1(A), (D)), were observed in the normal esophageal mucosa. The papilla (magenta arrows in Fig. 1(A), (D)) was easily distinguished by the centered collagen fibers and halo-like oval and layered epithelium surrounding it. Here, the cells and collagen fibers were visualized using TPEF and SHG signals, respectively, at a 750 nm excitation wavelength. The TPEF signals primarily originated from mitochondrial NADH [42] and appeared cyan to green in the images (Fig. 1(A)–(F)). In contrast, the remarkably shorter wavelength and lifetime of SHG signals gave them a blue with violet hints appearance in the fluorescence spectrum-coded images (Fig. 1(A)–(C)) and reddish-brown appearance in the fluorescence lifetime-coded images (Fig. 1(D)–(F)), respectively, while the lifetime became yellowish-green where the SHG signals were interwoven with TPEF (Fig. 1(D)).

In contrast to the normal esophageal mucosa, MD carcinoma featured clustered tumor cells (red arrows in Fig. 1(B), (E)) and increased collagen fibers (cyan arrows in Fig. 1(B), (E)). The tumor cells that appeared green in the images were identified according to the significantly higher nuclear-cytoplasmic ratio relative to the epithelial prickly cells. Compared to the orderly and tightly arranged normal epithelial cells that share a nearly uniform size in each layer, the tumor cells varied in size and shape, with inhomogeneous distribution and intercellular space

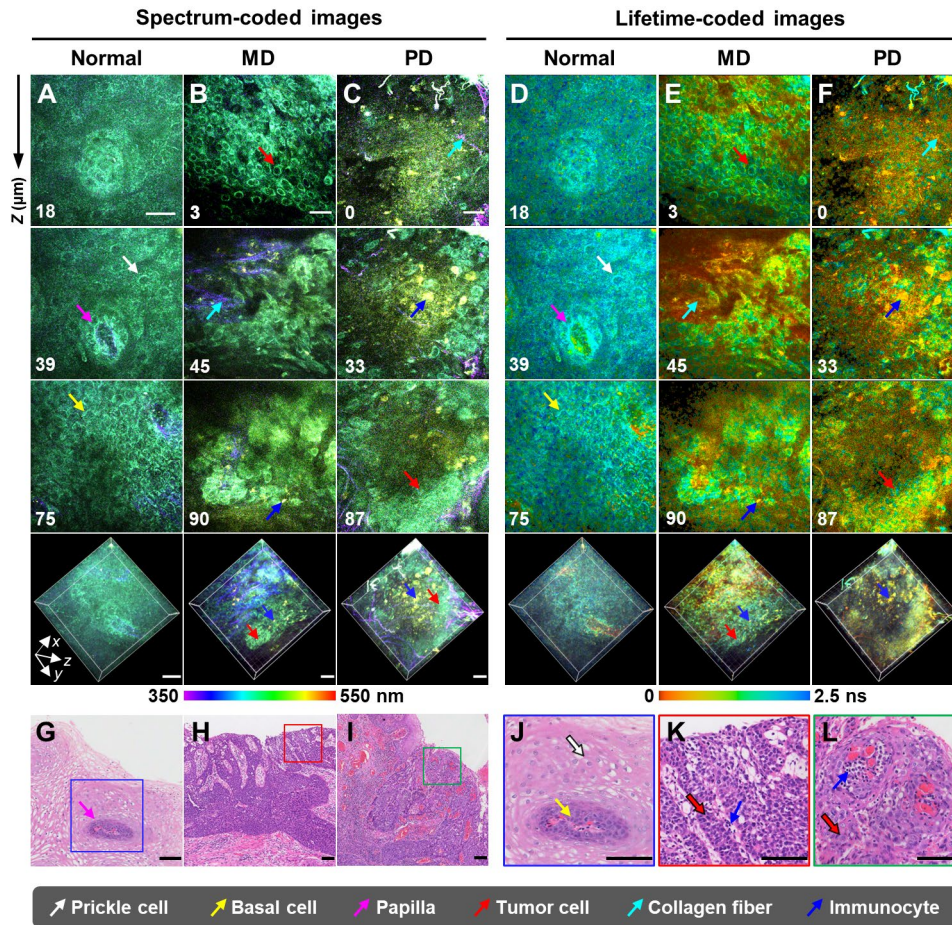


**Fig. 1.** Representative three-dimensional (3D) views of normal and cancerous human esophageal mucosae. (A–C) Fluorescence spectrum-coded images of normal tissue (A), moderately differentiated (MD) cancerous tissue (B), and poorly differentiated (PD) cancerous tissue (C). Two-dimensional (2D) images with different depths and corresponding 3D images are shown in the first three rows and the fourth row, respectively. The depth is labeled in the lower left corner of each panel. (D–F) Corresponding fluorescence lifetime-coded images. (G–I) H&E-stained histopathological slide images of normal tissue (G), MD cancerous tissue (H), and PD cancerous tissue (I). (J–L) Magnified images of the boxed areas of (G)–(I). Scale bars: 50  $\mu\text{m}$  in (A)–(C) and 100  $\mu\text{m}$  in (G)–(L). 2D images in (A) and (D) share the same scale bar, and the same goes for (B) and (E) as well as (C) and (F). The case of the 3D images is the same as that of the 2D images.

(Fig. 1(B), (E)). Moreover, some unique cells (blue arrows in Fig. 1(B), (E)), which appeared as bright yellow spots in the fluorescence spectrum-coded images, were occasionally captured in the cancerous area. These cells looked yellow to orange in the lifetime-coded images, and there was no distinct nucleus-cytoplasm boundary could be observed. These characteristics are obviously different from those of the normal cells (white and yellow arrows in Fig. 1 (A), (D)) and tumor cells (cyan arrows in Fig. 1(B), (E)). According to previous studies [44–46], we surmise that these unique cells might be immunocytes (consisting mainly of lymphocytes), and in addition to NADH, phospholipid was considered another possible contributor to their TPEF signals. In

terms of PD carcinoma, an anatomical structure resembling the MD was observed, but with more indistinct tumor cell borders and considerably increased immunocytes (Fig. 1(C), (F)).

We next compared the tumoral (T) and peritumoral (PT) tissues in patients with MD or PD cancer to further confirm the ability of MM-FLIM to discern ESCC (Fig. 2(A)–(D)). Considering individual differences among patients, particularly in terms of sex and age, a paired comparison of PT and T tissues from the same patient was chosen to provide a more reliable assessment. For MD carcinoma, stratified squamous epithelium resembling normal esophageal mucosa was observed in PT tissues (Fig. 2(A), (C)). Thus, T sites were easily discriminated from PT sites based on the aforementioned differences between normal mucosa and MD carcinoma (Fig. 1(A), (B), (D), (E)). In contrast, PT tissues of the PD carcinoma showed a distorted epithelium with an uneven surface and heteromorphic papillae. Nonetheless, the abundance of suspected immunocytes observed in the T sites render T tissues considerably different from the PT tissues in histology (Fig. 2(B), (D)). Indeed, the PD cancerous tissues varied widely from patient to patient and even from site to site, as shown in Figs. 1(C), (F), and 2(B), (D), but showed an increase in suspected immunocytes in common, relative to the normal mucosa, PT tissues, and MD carcinoma.

Compared to the gold standard H&E stained histopathological images (Fig. 1(G)–(L) and Fig. 2(E), (F)), the label-free MM-FLIM images described above (Fig. 1(A)–(F) and Fig. 2(A)–(D)) not only revealed consistent histological abnormalities of esophageal specimens, but also provided more specific identification of esophageal structural components, especially the collagen fibers and immunocytes (Figs. 1 and 2). The H&E technique generally unveils tissue histology by staining nuclei and cytoplasm in different colors. The morphological feature is almost the only criteria for it to distinguish different structural components. Contrastingly, the MM-FLIM can provide fluorescence spectrum and lifetime information as the “fingerprint” of different tissue intrinsic emitters for high-specificity characterization of esophageal structural components, in addition to the morphological information. The overall comparison (Fig. 1) and paired comparison (Fig. 2) together demonstrate that the various tissue intrinsic signals, coupled with the multidimensional detection ability and subcellular resolution of MM-FLIM, enable a fine histological depiction of normal and cancerous esophageal mucosae that underpins ESCC detection and grading.

### 3.2. Quantitative assessment of cell metabolism provides potential indicators of ESCC detection and grading

After unveiling the morphological variations of esophageal mucosa induced by ESCC, we attempted to further extract quantitative indicators for ESCC identification. As mentioned above, NADH was the primary origin of cellular autofluorescence. NADH serves as the major electron donor in cellular metabolic processes and exists in two forms in tissue: free and protein-bound. Free and protein-bound NADHs have emission maxima  $> 10$  nm apart (460 nm and 445 nm, respectively) and distinct fluorescence lifetimes ( $\sim 0.4$  ns and  $> 1$  ns, respectively) [43,47], and their ratio has been widely used as an indicator of the metabolic state of cells [30,48]. As normal epithelial cells showed variation in fluorescence spectrum and lifetime compared to cells within the cancerous tissue, as shown in Figs. 1(A)–(F) and 2(A)–(D), it seems possible to extract quantitative metabolic indicators from MM-FLIM data for ESCC identification. Therefore, we hypothesized that there are mainly two autofluorophore components in the cells, namely the free and protein-bound NADHs, as discussed above, and statistically quantified the spectrum and lifetime of cellular autofluorescence after segmenting cells from MM-FLIM images.

As shown in Fig. 3(A), the fluorescence spectrum exhibits remarkable red-shifts from normal, to MD carcinoma, to PD carcinoma, and the TPEF spectral ratio (the ratio of TPEF signals at 462.5–475 nm over that at 425–437.5 nm) that quantifies the red-shift provides an indicator that significantly differentiates the three groups (Fig. 3(B)). In terms of fluorescence lifetime analysis, we found that the mean fluorescence lifetime of free and protein-bound NADHs,  $\tau_{\text{mean}}$ , gradually decreases from normal, to MD carcinoma, to PD carcinoma, allowing for a



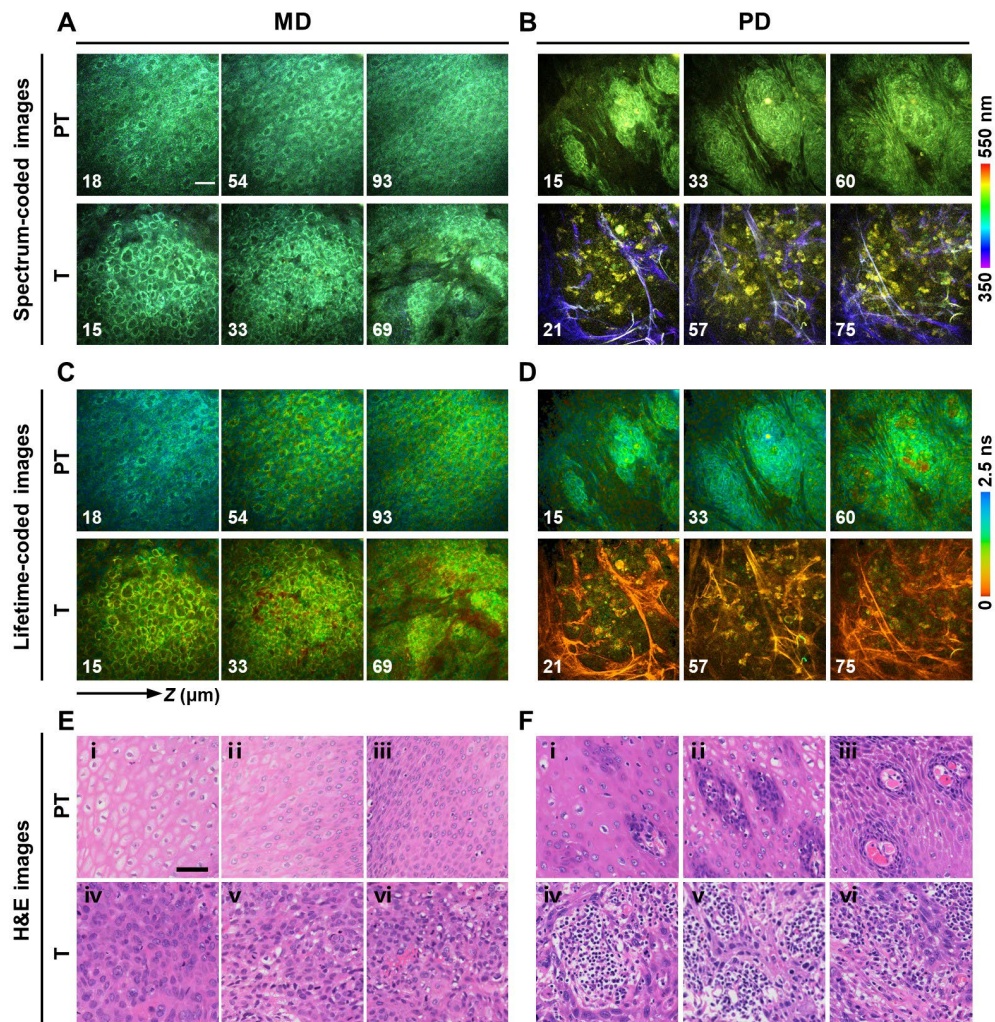


**Fig. 2.** Representative paired comparison of the three-dimensional views of peritumoral (PT) sites with tumoral (T) sites in the moderately differentiated (MD; A, C) and poorly differentiated (PD; B, D) cancerous human esophageal mucosae. (A, B) Fluorescence spectrum-coded images with different depths. The depth is labeled in the lower left corner of each panel. (C, D) Corresponding fluorescence lifetime-coded images. (E, F) H&E-stained histopathological slide images. Scale bars: 50  $\mu\text{m}$ . All of the images in (A)–(D) share the same scale bar, and all of the images in (E) and (F) share the same scale bar.

significant discrimination between normal and cancer (Fig. 3(C)). A consistent conclusion was drawn from the ratio of the two components,  $\alpha_1/\alpha_2$ , but with a contrary trend. The presented fluorescence spectrum and lifetime characteristics of cellular autofluorescence and the variation trend from normal to cancer are generally consistent with previous reports on NADH fluorescence [27,30]. These results suggest that the free NADH increased relative to the protein-bound NADH during ESCC occurrence and progression. This phenomenon is certainly consistent with the fact that neoplastic cells prefer to execute anaerobic glycolysis for energy production, rather than the oxidative phosphorylation commonly used by normal cells [49]. However, it may

also be associated with the increase of suspected immunocytes in MD and PD carcinomas, as lymphocytes were found to have a short NADH  $\tau_{\text{mean}}$  (0.6–0.7 ns) and the  $\tau_{\text{mean}}$  becomes even shorter when they are activated (0.55–0.6 ns) [45]. Other intrinsic emitters within the immunocytes, probably phospholipids [46], may also contribute to the variations in fluorescence spectrum and lifetime from normal to carcinomas.

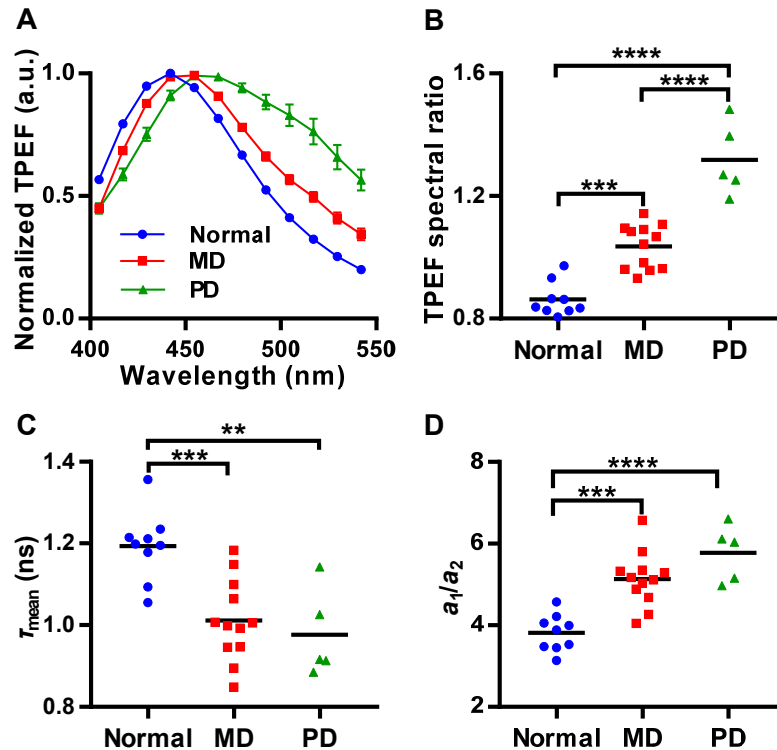


**Fig. 3.** Cell metabolism assessment in normal and cancerous human esophageal mucosae based on fluorescence spectrum (A, B) and lifetime (C, D) analysis of cellular autofluorescence. (A) The spectra of TPEF signals from cells. The error bars denote the SEM. (B) The ratio of TPEF intensity of a long-wavelength spectral channel ( $468.75 \pm 6.25$  nm) to that of a short-wavelength spectral channel ( $431.25 \pm 6.25$  nm). (C) The mean fluorescence lifetime of NADH. (D) The ratio of free to protein-bound NADH. MD: Moderately differentiated cancerous tissue, PD: Poorly differentiated cancerous tissue. The black solid lines in (B)–(D) denote the mean values. \*\* $0.001 < P < 0.01$ ; \*\*\* $0.0001 < P < 0.001$ ; \*\*\*\* $P < 0.0001$ ; one-way analysis of variance and Tukey's multiple comparison test (B–D).

As for paired comparison shown in Fig. 4, the T sites were clearly differentiated from corresponding PT tissues in terms of the fluorescence spectrum and lifetime as well as the associated parameters. The variation trends from PT to T tissues (Fig. 4) consist with those from normal tissues to carcinoma (Fig. 3). In addition, gaps between PT tissues and the normal group were observed, particularly in the fluorescence lifetime (Fig. 4). These results (Fig. 4), coupled with the overall comparison (Fig. 3) presented above, demonstrate that the MM-FLIM is sensitive to the metabolic variation induced by ESCC. The TPEF spectrum, TPEF spectral ratio,  $\tau_{\text{mean}}$ , and  $\alpha_1/\alpha_2$  derived from MM-FLIM images can perceive metabolic differences among tumor cells, immunocytes, and normal epithelium; on the strength of this ability, they are promising indicators of ESCC detection and grading.

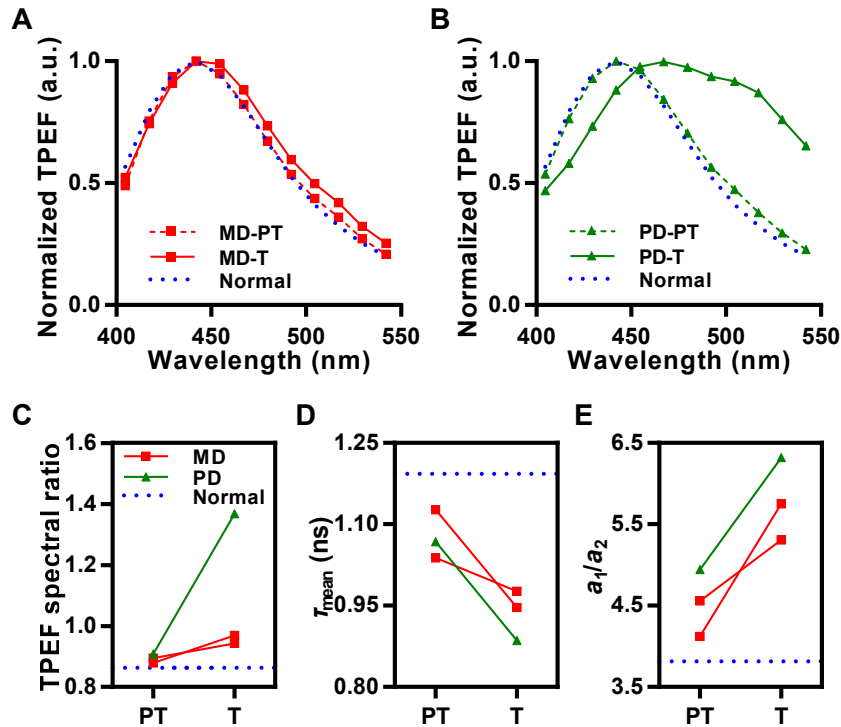


**Fig. 4.** Representative paired comparison of the cellular autofluorescence spectral and lifetime characteristics of peritumoral (PT) sites with tumoral (T) sites in the moderately differentiated (MD) and poorly differentiated (PD) cancerous human esophageal mucosae. (A, B) Fluorescence spectra of cellular TPEF signals from MD (A) and PD (B) cancerous tissues. (C) The ratio of TPEF intensity of a long-wavelength spectral channel ( $468.75 \pm 6.25$  nm) to that of a short-wavelength spectral channel ( $431.25 \pm 6.25$  nm). (D) The mean fluorescence lifetime of NADH. (E) The ratio of free to protein-bound NADH. The red lines denote MD; the green lines denote PD. The average values of normal tissues are presented as blue dotted lines for comparison. Note that the data shown in (A) and (B) are from a single MD patient and a single PD patient, respectively. Each pair of data points connected by a solid line in (C)-(E) are from the same patient.

### 3.3. Quantification of stromal fibers unveils promising supplementary indicators of ESCC

In addition to cells, we also investigated the stromal fibers. Collagen, which participates in cancer fibrosis, increases tumor stiffness, regulates tumor immunity, and promotes metastasis, is a major component of the tumor microenvironment [50]. It is clear that collagen fibers are increased in cancerous tissues relative to the normal and PT tissues (Figs. 1 and 2), and thus appear to be a promising indicator of ESCC. As collagen fibers are specifically detected using SHG signals, we quantified their relative content directly by SHG/TPEF (the ratio of the SHG spectral peak over the TPEF peak). Despite the scattered distribution of PD data, the ratio gradually increases from normal, to MD, to PD on average (Fig. 5(A)). The PT tissues are similar to normal tissues with SHG/TPEF values close to 0, remarkably lower than those of T sites (Fig. 5(B)). A consistent conclusion can be drawn from the paired comparison (Fig. 5(C)).

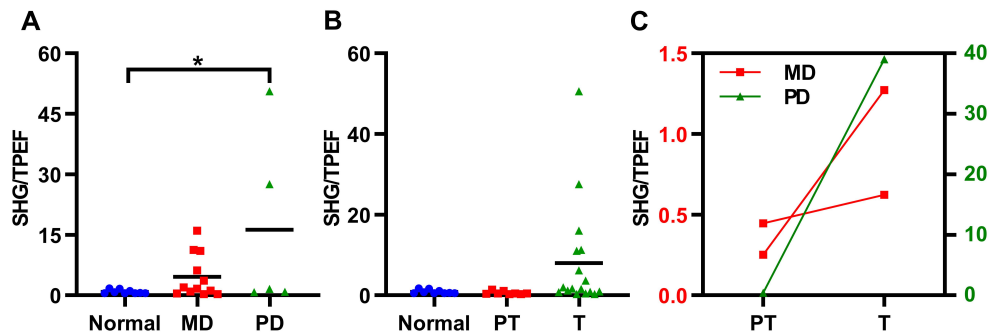


**Fig. 5.** Assessment of the relative content of collagen fibers in normal and cancerous human esophageal mucosae based on SHG/TPEF (the ratio of signals from the spectral channel with maximum SHG [ $381.25 \pm 6.25$  nm] to those from the channel with maximum TPEF [ $443.75 \pm 6.25$  nm,  $456.25 \pm 6.25$  nm, or  $468.75 \pm 6.25$  nm]). (A) Comparison of normal tissues, moderately differentiated (MD) cancerous tissues, and poorly differentiated (PD) cancerous tissues. (B) Comparison of normal tissues with peritumoral (PT) and tumoral (T) sites in cancerous tissues (the data of MD and PD were combined in analysis). The black solid lines in (A) and (B) denote the mean values.  $*0.01 < P < 0.05$ ; one-way analysis of variance and Tukey's multiple comparison test (A, B). (C) Paired comparison of PT and T sites. The left (red) and right (green) ordinates correspond to the data of MD and PD, respectively. Note that each pair of data points connected by a solid line are from the same patient.

Fragmented or short elastin fibers (red arrowheads in Fig. 6(A)–(D)) interweaving with collagen fibers were observed in most T sites, especially around the tumor cell nests. In normal esophageal mucosa, other than the superficial epithelium and papillae, the elastin fibers appear in rather deeper layers [44], which are beyond the maximum imaging depth of label-free MPM. Therefore, the presence of elastin fibers in the shallow esophageal mucosa or in the MPM images could be used as an indicator of ESCC. Moreover, even at deep layers, the distinct morphology of elastin fibers in normal and cancerous tissues allows straightforward identification of ESCC. For instance, in the submucosa, compared to the disordered and fragmented short elastin fibers around tumor cell clusters, regularly packed long and curly elastin fibers are in the majority in normal tissues [51].

Overall, the stromal collagen and elastin fibers can be easily identified by their fiber-like structures revealed in the MM-FLIM images, and radically differentiated from each other relying on the fluorescence spectrum (Fig. 6(A), (B), the collagen and elastin fibers appear blue with violet hints and light yellow, respectively) and lifetime (Fig. 6(C), (D), the collagen and elastin fibers show reddish-brown and amber appearances, respectively). On top of that, the derived SHG/TPEF and presence of fragmented elastin fibers are promising supplementary indicators of ESCC, although T sites usually vary widely from site to site. Contrastingly, it is really difficult to distinguish collagen fibers from elastin fibers in the H&E-stained images, although fiber-like structures are observable as well (Fig. 6(E), (F)). Accurate discrimination of these stromal fibers in clinics requires more specific histopathological staining.

#### 3.4. Specific identification of keratin pearls further contributes to the discrimination and early detection of ESCC

The keratin pearl, which is composed of concentric rings of squamous cells showing gradual keratinization, has long been used as a histopathological marker to guide ESCC diagnosis [31,32,52]. Specifically, the degree of keratinization dramatically changes with ESCC occurrence



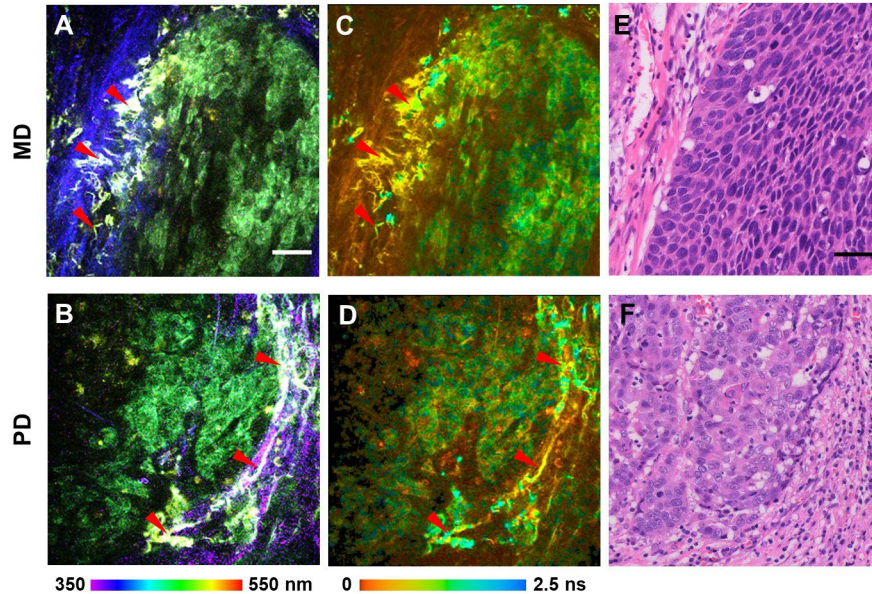


**Fig. 6.** Elastin fibers (red arrowheads) are present in cancerous human esophageal mucosae. Representative (A, B) fluorescence spectrum-coded images, (C, D) corresponding fluorescence lifetime-coded images, and (E, F) H&E-stained histopathological slide images are shown. MD: Moderately differentiated cancerous tissue (A, C, E); PD: Poorly differentiated cancerous tissue (B, D, F). Scale bars: 50  $\mu$ m. (A)–(D) share the same scale bar, and (E) and (F) share the same scale bar.

and progression. The normal esophageal squamous epithelium is nonkeratinizing, whereas prominent keratin pearls are frequently present in the well-differentiated (WD) carcinoma. Compared to WD ESCC, only occasional keratin pearls appear in the MD carcinoma, and in terms of PD ESCC, keratinization is minimal [53]. Therefore, accurate identification of keratin pearls may substantially benefit the early detection and grading of ESCC. Moreover, ESCC and adenocarcinoma are the two major histologic types of esophageal cancer [53]. The presence of keratin pearls can be used as a criterion to discriminate ESCC from adenocarcinoma [32,54].

As shown in Fig. 7(A), (B), we captured keratin pearls (yellow arrowheads) in the nest of neoplastic cells in individual cases of MD ESCC using MM-FLIM. We did not include WD carcinoma in our study due to the unmet need of early ESCC detection and accordingly the rarity of WD carcinoma cases in clinics. MM-FLIM enables accurate and quantitative identification of keratin pearls mainly according to their oval shape and the obvious red shift in the fluorescence spectrum relative to surrounding cells (Fig. 7(A)). The fluorescence lifetime also helps to distinguish keratin pearls from structural components like collagen fibers, despite the minimal lifetime difference between keratin pearls and tumor cells around them (Fig. 7(B)). The identified keratin pearls in the MM-FLIM images (Fig. 7(A), (B)) were confirmed using the gold standard H&E-stained histopathological images (Fig. 7(D)).

Notably, the keratin pearls (yellow arrowheads in Fig. 7(D)) in H&E-stained images look very similar to the papillae (blue arrowheads in Fig. 7(C)) sometimes. Therefore, the discrimination between keratin pearls and papillae in the H&E images relies primarily on accurate identification of their surrounding tissues, i.e., tumor cells and stratified squamous epithelial cells, respectively (Fig. 7(C), (D)). However, at the early stage of ESCC, the cancer cells are generally well

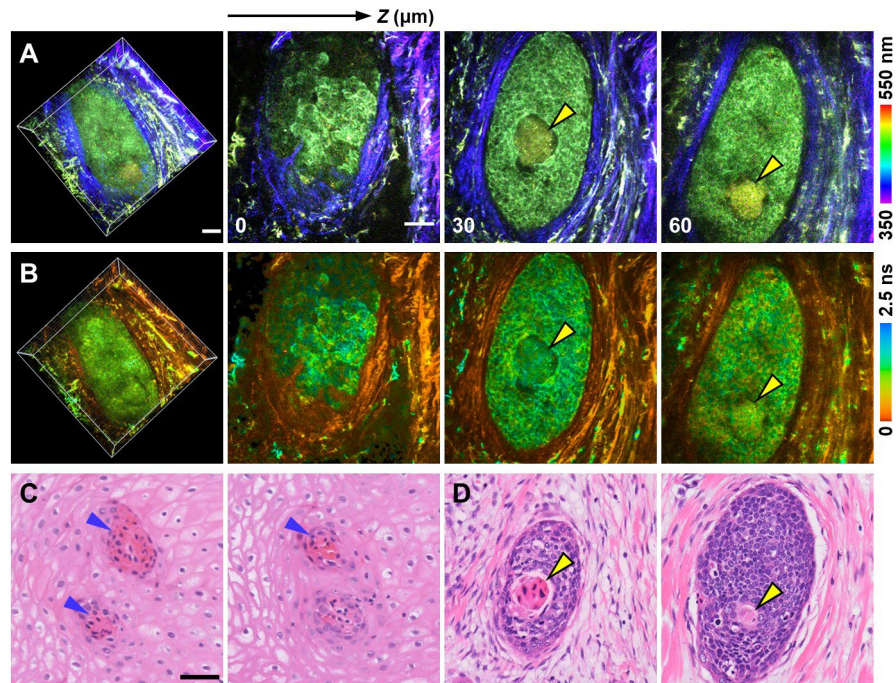


**Fig. 7.** Representative three-dimensional (3D) structures of keratin pearls (yellow arrowheads) presented in moderately differentiated (MD) cancerous human esophageal mucosa. (A) Fluorescence spectrum-coded 3D image and corresponding two-dimensional (2D) images with different depths. The depth of each panel is labeled in the lower left corner. (B) Corresponding fluorescence lifetime-coded images. (C, D) Papillae (blue arrowheads) (C) and keratin pearls (D) in H&E-stained histopathological slide images. Scale bars: 50  $\mu\text{m}$ . 3D images in (A) and (B) share the same scale bar, and the same goes for the 2D images. All the images in (C) and (D) share the same scale bar.

differentiated and resemble normal cells in appearance. In contrast to H&E images, the MM-FLIM features multi-dimensional (3D fluorescence intensity, spectrum, and lifetime) imaging ability. This unique ability not only allows direct identification of keratin pearls (Fig. 7(A)) but also provides quantitative discrimination between carcinomas and normal tissues (Figs. 1–6), and thus has the potential to substantially benefit the early detection of ESCC.

### 3.5. Systematic comparison of the various structural components presented in normal and cancerous mucosae confirms the potential of MM-FLIM for discerning ESCC

We have demonstrated that the MM-FLIM is capable of characterizing the various structural components presented in normal and cancerous esophageal mucosae, including the normal cells, tumor cells, collagen fibers, elastin fibers, and keratin pearls. As the cornerstone of MM-FLIM-based ESCC detection and grading, this has not yet been directly illustrated through a quantitative comparison of the aforementioned structures. To this end, we segmented these structures from the MM-FLIM images and performed a systematic difference analysis of their fluorescence spectra and lifetimes. The derived optical characteristics of the structures (Fig. 8) are found generally consistent with that of the endogenous fluorophores [55–57] mainly contained in the structures. The comparison shows that all the structures can be distinguished from one other according to the fluorescence spectrum (Fig. 8(A)). The same goes for the fluorescence lifetime

with only one exception, i.e., the tumor cells and keratin pearls are indistinguishable (Fig. 8(B)). A hypothesis of two autofluorophore components was also used for acellular structures in the fluorescence lifetime calculation here for fair comparison with cellular autofluorescence (mainly from free and protein-bound NADHs [47]), and the mean fluorescence lifetime of the two components was eventually used for comparison. These results finally confirm the ability of MM-FLIM to specifically identify the structural components of normal and cancerous esophageal mucosae. On the strength of this ability and its derivatives, namely the qualitative and quantitative ESCC indicators discussed in Sections 3.1–3.4, MM-FLIM shows tremendous potential for ESCC detection and grading (Table 1).

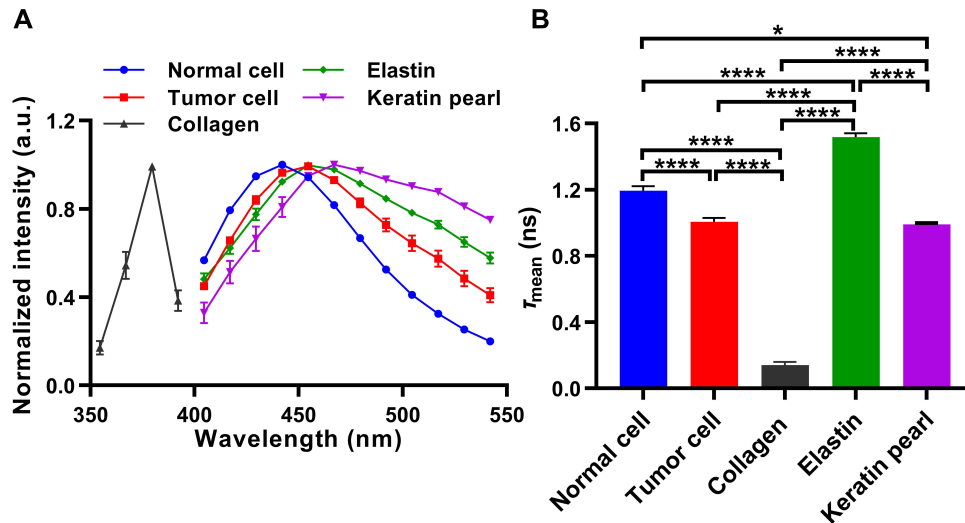


**Fig. 8.** Comparison of (A) fluorescence spectra and (B) fluorescence lifetimes of different structural components presented in normal and cancerous human esophageal mucosae. Notably, the normal cell represents cells from normal tissues, not including peritumoral tissues. The tumor cells represent cells in moderately and poorly differentiated cancerous tissues, and the suspected immunocytes were not specifically excluded. The error bars denote the SEM.  $*0.01 < P < 0.05$ ;  $****P < 0.0001$ ; one-way analysis of variance and Tukey's multiple comparison test.

Among these MM-FLIM-based ESCC indicators (Table 1), the most crucial ones are cell metabolism parameters (Figs. 3 and 4), as cell is the core component of normal and cancerous esophageal epithelium and the tumor cells prefer quite distinct metabolic pathway for energy production from the normal cells [49]. Even the basal cells (yellow arrows in Fig. 1(A), (D), and J, a type of normal esophageal epithelial cell) and the basaloid tumor cells (red arrows in Fig. 1(B), (E), and (K)) that with similar morphology, can be easily distinguished from each other according to the cell metabolism parameters. For other indicators, there are some limitations should be stated. The relative content of collagen fibers, characterized by SHG/TPEF (Fig. 5), varies from one site to another. Accurate assessment of it requires sufficient sampling. The elastin fibers and keratin pearls were observed with relatively lower probability in ESCC tissue. To capture these occasional structures, large field-of-view imaging would be desired. Nonetheless, these two structure components can be clearly identified by integrating the morphological, fluorescence spectrum, and fluorescence lifetime information (Figs. 6–8 and Table 1), and indicate the ESCC simply by their presence (Table 1). Moreover, the keratin pearl is a generally accepted specific indicator of WD and MD ESCC and can be used to discriminate ESCC from the esophageal adenocarcinoma [32,53,54]. Overall, indicators related to the stromal fibers and keratinization



**Table 1. Summary of MM-FLIM-based potential indicators for ESCC detection and grading.**

Structural components	Structural component identification		Potential indicators for ESCC detection and grading		
	Qualitative feature	Quantitative feature	Normal	MD	PD
Tumor cell	High nuclear-cytoplasmic ratio; varied size and shape; inhomogeneous distribution [Fig. 1B, C, E, F]	$SR$ $1.12 \pm 0.04$	- $SR$ $0.86 \pm 0.02$	+ $SR$ ( $\uparrow$ ) $1.04 \pm 0.02$	+ $SR$ ( $\uparrow\uparrow$ ) $1.32 \pm 0.05$
		$T_{mean}$ $1.00 \pm 0.02$ ns	$T_{mean}$ $1.19 \pm 0.03$ ns	$T_{mean}$ ( $\downarrow$ ) $1.01 \pm 0.03$ ns	$T_{mean}$ ( $\downarrow$ ) $0.98 \pm 0.05$ ns
		$\alpha_1/\alpha_2$ $5.32 \pm 0.17$	$\alpha_1/\alpha_2$ $3.82 \pm 0.15$	$\alpha_1/\alpha_2$ ( $\uparrow$ ) $5.13 \pm 0.19$	$\alpha_1/\alpha_2$ ( $\uparrow$ ) $5.78 \pm 0.31$
		[Fig. 3B–D, MD+PD]	[Fig. 3B–D, Normal]	[Fig. 3B–D, MD]	[Fig. 3B–D, PD]
Collagen fiber	Fiber-like structure [Fig. 1A–F]	$\lambda_{em} = 1/2\lambda_{ex}$ $T_{mean}$ $0.14 \pm 0.02$ ns	+ SHG/TPEF $0.87 \pm 0.16$	+ SHG/TPEF $4.56 \pm 1.54$	+ SHG/TPEF ( $\uparrow$ ) $16.24 \pm 10.00$
		[SHG signal; Fig. 8]	[Fig. 5A, Normal]	[Fig. 5A, MD]	[Fig. 5A, PD]
Elastin fiber	Fiber-like structure [Fig. 6 A–D]	$SR$ $1.28 \pm 0.06$	-	+	+
		$T_{mean}$ $1.52 \pm 0.02$ ns			
		[Fig. 8]			
Keratin pearl	Pearl-like multicellular structure; individual cells can't be distinguished [Fig. 7A, B]	$SR$ $1.51 \pm 0.13$	-	+	-
		$T_{mean}$ $0.99 \pm 0.01$ ns			
		[Fig. 8]			

**Notes:**

MM-FLIM: Multispectral multiphoton fluorescence lifetime imaging microscopy; ESCC: Esophageal squamous cell carcinoma; MD: Moderately differentiated ESCC; PD: Poorly differentiated ESCC;  $SR$ : TPEF spectral ratio;  $\lambda_{ex}$ : Excitation wavelength;  $\lambda_{em}$ : Emission wavelength; + and -: Presence and absence of a given structural component, respectively;  $\uparrow$  and  $\downarrow$ : Statistically significant increase and decrease relative to the normal cell or tissue, respectively.

The qualitative features and quantitative data are from MM-FLIM images and corresponding fluorescence spectrum and lifetime statistics, respectively. The figure numbers of representative images that contain the qualitative features are provided within the square brackets below the feature descriptions. The quantitative data are presented as the mean  $\pm$  SEM, and the source figure numbers are marked below them as well. Note that  $SR$  values of the elastin fiber and keratin pearl were not directly provided in Fig. 8 but calculated from the fluorescence spectra shown in Fig. 8(A).

also provide important information for ESCC detection and grading, in addition to the cell metabolism indicators. Combining these indicators together would empower more accurate ESCC identification.

#### 4. Conclusion

In summary, by performing systematic MM-FLIM imaging on clinical specimens of different ESCC grades, we unveiled mucosal variations induced by ESCC and derived potential indicators for ESCC detection and grading. First, differences among normal tissues, MD carcinoma, and PD carcinoma in terms of morphology and structural composition were presented by creating a fluorescence spectrum- and lifetime-coded images. Second, quantifying the spectrum and lifetime of cellular autofluorescence provided metabolic indicators of ESCC identification and grading. Third, assessing collagen fiber content using SHG/TPEF and discriminating elastin fibers based on their distinct fluorescence spectrum and lifetime further unveiled supplementary indicators of ESCC. Finally, keratin pearls, which play critical roles in the pathological typing of esophageal cancer and the early detection of ESCC, were specifically discerned in the MM-FLIM images. From these, we observed the significant potential of the demonstrated MM-FLIM and the derived indicators for histopathological examination of ESCC. Since the imaging is multidimensional, slicing-free, and label-free, miniaturizing the imaging system for endoscopic probing in the future would probably empower noninvasive histopathological evaluation of ESCC. On the other



hand, the sample size was limited and cases with WD carcinoma were excluded from our study due to the difficulties with specimen collection. Further studies involving more cases as well as the future *in vivo* endoscopy will be required to robustly assess the clinical utility of the proposed method. Besides, tumor heterogeneity analysis [58] may provide more precise characterization of ESCC and significantly benefit ESCC diagnosis and related basic research. Future study taking this important point into consideration is also desired.

**Funding.** National Natural Science Foundation of China (92159104, 82071972, 91959121); Basic and Applied Basic Research Foundation of Guangdong Province (2020B121201010); Scientific Instrument Innovation Team of the Chinese Academy of Sciences (GJJSTD20210003); Youth Innovation Promotion Association of the Chinese Academy of Sciences (2023377); Shenzhen Fundamental Research Program (RCYX20210609104445093, RCJC20200714114433058, ZDSY20130401165820357).

**Disclosures.** The authors declare no conflicts of interest.

**Data availability.** All data needed to evaluate the conclusions in the paper are presented in the paper and/or the Supplementary Materials. Correspondence and requests for materials should be addressed to Hui Li (email: hui.li@siat.ac.cn), Wei Zheng (email: zhengwei@siat.ac.cn), or Xi Li (email: lixi122188@sina.com).

**Supplemental document.** See [Supplement 1](#) for supporting content.

## References

1. H. Sung, J. Ferlay, R. L. Siegel, M. Laversanne, I. Soerjomataram, A. Jemal, and F. Bray, "Global Cancer Statistics 2020: GLOBOCAN estimates of incidence and mortality worldwide for 36 cancers in 185 countries," *Ca-Cancer J. Clin.* **71**(3), 209–249 (2021).
2. W. Hatta, T. Koike, Y. Ogata, Y. Kondo, N. Ara, K. Uno, N. Asano, A. Imatani, and A. Masamune, "Comparison of magnifying endoscopy with blue light imaging and narrow band imaging for determining the invasion depth of superficial esophageal squamous cell carcinoma by the Japanese esophageal society's intrapapillary capillary loop classification," *Diagnostics* **11**(11), 1941 (2021).
3. D. C. Codipilly, Y. Qin, S. M. Dawsey, J. Kisiel, M. Topazian, D. Ahlquist, and P. G. Iyer, "Screening for esophageal squamous cell carcinoma: recent advances," *Gastrointest. Endosc.* **88**(3), 413–426 (2018).
4. P. Lao-Sirieix and R. C. Fitzgerald, "Screening for oesophageal cancer," *Nat. Rev. Clin. Oncol.* **9**(5), 278–287 (2012).
5. H. Kondo, H. Fukuda, H. Ono, T. Gotoda, D. Saito, K. Takahiro, K. Shirao, H. Yamaguchi, and S. Yoshida, "Sodium thiosulfate solution spray for relief of irritation caused by Lugol's stain in chromoendoscopy," *Gastrointest. Endosc.* **53**(2), 199–202 (2001).
6. F. P. Borges Martins Thuler, G. A. de Paulo, and A. P. Ferrari, "Chemical esophagitis after chromoendoscopy with Lugol's solution for esophageal cancer: case report," *Gastrointest. Endosc.* **59**(7), 925–926 (2004).
7. A. Sreedharan, B. Rembacken, and O. Rotimi, "Acute toxic gastric mucosal damage induced by Lugol's iodine spray during chromoendoscopy," *Gut* **54**(6), 886–887 (2005).
8. J. Myung Park, I. Seok Lee, J. Young Kang, C. Nyol Paik, Y. Kyung Cho, S. Woo Kim, M.-G. Choi, and I.-S. Chung, "Acute esophageal and gastric injury: complication of Lugol's solution," *Scand. J. Gastroenterol.* **42**(1), 135–137 (2007).
9. H. Osawa and H. Yamamoto, "Present and future status of flexible spectral imaging color enhancement and blue laser imaging technology," *Dig. Endosc.* **26**, 105–115 (2014).
10. M. Ebi, T. Shimura, T. Yamada, T. Mizushima, K. Itoh, H. Tsukamoto, K. Tsuchida, Y. Hirata, K. Murakami, H. Kanie, S. Nomura, H. Iwasaki, M. Kitagawa, S. Takahashi, and T. Joh, "Multicenter, prospective trial of white-light imaging alone versus white-light imaging followed by magnifying endoscopy with narrow-band imaging for the real-time imaging and diagnosis of invasion depth in superficial esophageal squamous cell carcinoma," *Gastrointest. Endosc.* **81**(6), 1355–1361.e2 (2015).
11. H. Liu, Y. Li, T. Yu, Y. Zhao, J. Zhang, X. Zuo, C. Li, J. Zhang, Y. Guo, and T. Zhang, "Confocal laser endomicroscopy for superficial esophageal squamous cell carcinoma," *Endoscopy* **41**(02), 99–106 (2009).
12. V. Shavlokhova, C. Flechtenmacher, S. Sandhu, M. Pilz, M. Vollmer, J. Hoffmann, M. Engel, and C. Freudspurger, "Detection of oral squamous cell carcinoma with ex vivo fluorescence confocal microscopy: Sensitivity and specificity compared to histopathology," *J. Biophotonics* **13**(9), e202000100 (2020).
13. O. Pech, T. Rabenstein, H. Manner, M. C. Petrone, J. Pohl, M. Vieth, M. Stolte, and C. Ell, "Confocal laser endomicroscopy for in vivo diagnosis of early squamous cell carcinoma in the esophagus," *Clin. Gastroenterol. Hepatol.* **6**(1), 89–94 (2008).
14. H. Mashimo, S. R. Gordon, and S. K. Singh, "Advanced endoscopic imaging for detecting and guiding therapy of early neoplasias of the esophagus," *Ann. N.Y. Acad. Sci.* **1482**(1), 61–76 (2020).
15. P. E. Paull, B. J. Hyatt, W. Wassef, and A. H. Fischer, "Confocal laser endomicroscopy: A primer for pathologists," *Arch. Pathol. Lab. Med.* **135**(10), 1343–1348 (2011).
16. W. R. Zipfel, R. M. Williams, R. Christie, A. Y. Nikitin, B. T. Hyman, and W. W. Webb, "Live tissue intrinsic emission microscopy using multiphoton-excited native fluorescence and second harmonic generation," *Proc. Natl. Acad. Sci. U. S. A.* **100**(12), 7075–7080 (2003).

17. W. Liang, G. Hall, B. Messerschmidt, M.-J. Li, and X. Li, "Nonlinear optical endomicroscopy for label-free functional histology in vivo," *Light: Sci. Appl.* **6**(11), e17082 (2017).
18. J. Li, M. N. Wilson, A. J. Bower, M. Marjanovic, E. J. Chaney, R. Barkalifa, and S. A. Boppart, "Video-rate multimodal multiphoton imaging and three-dimensional characterization of cellular dynamics in wounded skin," *J. Innov. Opt. Health Sci.* **13**(02), 2050007 (2020).
19. Y. Li, B. Shen, G. Zou, R. Hu, Y. Pan, J. Qu, and L. Liu, "Super-multiplex nonlinear optical imaging unscrambles the statistical complexity of cancer subtypes and tumor microenvironment," *Adv. Sci.* **9**(5), 2104379 (2022).
20. F. Helmchen and W. Denk, "Deep tissue two-photon microscopy," *Nat. Methods* **2**(12), 932–940 (2005).
21. E. E. Hoover and J. A. Squier, "Advances in multiphoton microscopy technology," *Nat. Photonics* **7**(2), 93–101 (2013).
22. A. Dilipkumar, A. Al-Shemmary, L. Kreiß, K. Cvecek, B. Carlé, F. Knieling, J. Gonzales Menezes, O.-M. Thoma, M. Schmidt, M. F. Neurath, M. Waldner, O. Friedrich, and S. Schürmann, "Label-free multiphoton endomicroscopy for minimally invasive in vivo imaging," *Adv. Sci.* **6**(8), 1801735 (2019).
23. Y. Ouyang, Y. Liu, Z. M. Wang, Z. Liu, and M. Wu, "FLIM as a promising tool for cancer diagnosis and treatment monitoring," *Nanomicro Lett.* **13**(1), 133 (2021).
24. P. H. Lakner, M. G. Monaghan, Y. Möller, M. A. Olayioye, and K. Schenke-Layland, "Applying phasor approach analysis of multiphoton FLIM measurements to probe the metabolic activity of three-dimensional in vitro cell culture models," *Sci. Rep.* **7**(1), 42730 (2017).
25. M. Popleteeva, K. T. Haas, D. Stoppa, L. Pancheri, L. Gasparini, C. F. Kaminski, L. D. Cassidy, A. R. Venkiteswaran, and A. Esposito, "Fast and simple spectral FLIM for biochemical and medical imaging," *Opt. Express* **23**(18), 23511–23525 (2015).
26. E. Duran-Sierra, S. Cheng, R. Cuenca-Martinez, B. Malik, K. C. Maitland, Y. S. Lisa Cheng, J. Wright, B. Ahmed, J. Ji, M. Martinez, M. Al-Khalil, H. Al-Enazi, and J. A. Jo, "Clinical label-free biochemical and metabolic fluorescence lifetime endoscopic imaging of precancerous and cancerous oral lesions," *Oral Oncol* **105**, 104635 (2020).
27. M. C. Skala, K. M. Riching, A. Gendron-Fitzpatrick, J. Eickhoff, K. W. Eliceiri, J. G. White, and N. Ramanujam, "In vivo multiphoton microscopy of NADH and FAD redox states, fluorescence lifetimes, and cellular morphology in precancerous epithelia," *Proc. Natl. Acad. Sci. U. S. A.* **104**(49), 19494–19499 (2007).
28. Y.-F. Shen, M.-R. Tsai, S.-C. Chen, Y.-S. Leung, C.-T. Hsieh, Y.-S. Chen, F.-L. Huang, R. P. Obena, M. M. L. Zulueta, H.-Y. Huang, W.-J. Lee, K.-C. Tang, C.-T. Kung, M.-H. Chen, D.-B. Shieh, Y.-J. Chen, T.-M. Liu, P.-T. Chou, and C.-K. Sun, "Imaging endogenous bilirubins with two-photon fluorescence of bilirubin dimers," *Anal. Chem.* **87**(15), 7575–7582 (2015).
29. S. K. Teh, W. Zheng, S. Li, D. Li, Y. Zeng, Y. Yang, and J. Y. Qu, "Multimodal nonlinear optical microscopy improves the accuracy of early diagnosis of squamous intraepithelial neoplasia," *J. Biomed. Opt.* **18**(3), 036001 (2013).
30. X. Li, H. Li, X. He, T. Chen, X. Xia, C. Yang, and W. Zheng, "Spectrum-and time-resolved endogenous multiphoton signals reveal quantitative differentiation of premalignant and malignant gastric mucosa," *Biomed. Opt. Express* **9**(2), 453–471 (2018).
31. D. Savant, Q. Zhang, and Z. Yang, "Squamous neoplasia in the esophagus," *Arch. Pathol. Lab. Med.* **145**(5), 554–561 (2021).
32. M. W. Taggart, A. Rashid, W. A. Ross, and S. C. Abraham, "Oesophageal hyperkeratosis: clinicopathological associations," *Histopathology* **63**(4), 463–473 (2013).
33. R. Weigert, *Advances in Intravital Microscopy: From Basic to Clinical Research* (Springer, 2014), pp. 305–370.
34. W. Liang, D. Chen, H. Guan, H.-C. Park, K. Li, A. Li, M.-J. Li, I. Gannot, and X. Li, "Label-free metabolic imaging in vivo by two-photon fluorescence lifetime endomicroscopy," *ACS Photonics* **9**(12), 4017–4029 (2022).
35. K. König, "Clinical multiphoton tomography," *J. Biophotonics* **1**(1), 13–23 (2008).
36. R. Patalay, C. Talbot, Y. Alexandrov, I. Munro, M. A. Neil, K. König, P. M. French, A. Chu, G. W. Stamp, and C. Dunsby, "Quantification of cellular autofluorescence of human skin using multiphoton tomography and fluorescence lifetime imaging in two spectral detection channels," *Biomed. Opt. Express* **2**(12), 3295–3308 (2011).
37. M. Balu, K. M. Kelly, C. B. Zachary, R. M. Harris, T. B. Krasieva, K. König, A. J. Durkin, and B. J. Tromberg, "Distinguishing between benign and malignant melanocytic nevi by in vivo multiphoton microscopy: benign and malignant melanocytic nevi imaging by in vivo MPM," *Cancer Res.* **74**(10), 2688–2697 (2014).
38. H. Li, Y. Yin, F. Xiang, J. Yu, T. Wu, L. Liu, J. Liao, and W. Zheng, "Label-free characterization of ischemic cerebral injury using intravital two-photon excitation fluorescence lifetime imaging microscopy," *J. Phys. D: Appl. Phys.* **54**(11), 114001 (2021).
39. J. J. Engelhardt, B. Boldajipour, P. Beemiller, P. Pandurangi, C. Sorensen, Z. Werb, M. Egeblad, and M. F. Krummel, "Marginating dendritic cells of the tumor microenvironment cross-present tumor antigens and stably engage tumor-specific T cells," *Cancer Cell* **21**(3), 402–417 (2012).
40. H. J. Park, "Pathobiology of human disease malignant epithelial tumors of skin," 1173–1181 (2014).
41. M. Malak, J. James, J. Grantham, and M. B. Ericson, "Contribution of autofluorescence from intracellular proteins in multiphoton fluorescence lifetime imaging," *Sci. Rep.* **12**(1), 16584 (2022).
42. A. Klinger, R. Orzekowsky-Schroeder, D. von Smolinski, M. Blessenohl, A. Schueth, N. Koop, G. Huettmann, and A. Gebert, "Complex morphology and functional dynamics of vital murine intestinal mucosa revealed by autofluorescence 2-photon microscopy," *Histochem. Cell Biol.* **137**(3), 269–278 (2012).

43. P. M. Schaefer, S. Kalinina, A. Rueck, C. A. von Arnim, and B. von Einem, "NADH autofluorescence—a marker on its way to boost bioenergetic research," *Cytometry* **95**(1), 34–46 (2019).
44. W. Pawlina and M. H. Ross, *Histology: A Text and Atlas: With Correlated Cell and Molecular Biology* (Lippincott Williams & Wilkins, 2018).
45. A. J. Walsh, K. P. Mueller, K. Tweed, I. Jones, C. M. Walsh, N. J. Piscopo, N. M. Niemi, D. J. Pagliarini, K. Saha, and M. C. Skala, "Classification of T-cell activation via autofluorescence lifetime imaging," *Nat. Biomed. Eng.* **5**(1), 77–88 (2020).
46. W. Hu and L. Fu, "Simultaneous characterization of pancreatic stellate cells and other pancreatic components within three-dimensional tissue environment during chronic pancreatitis," *J. Biomed. Opt.* **18**(5), 056002 (2013).
47. J. A. Palero, A. N. Bader, H. S. de Bruijn, H. J. Sterenborg, and H. C. Gerritsen, "In vivo monitoring of protein-bound and free NADH during ischemia by nonlinear spectral imaging microscopy," *Biomed. Opt. Express* **2**(5), 1030–1039 (2011).
48. R. Datta, C. Heylman, S. C. George, and E. Gratton, "Label-free imaging of metabolism and oxidative stress in human induced pluripotent stem cell-derived cardiomyocytes," *Biomed. Opt. Express* **7**(5), 1690–1701 (2016).
49. I. Martínez-Reyes and N. S. Chandel, "Cancer metabolism: looking forward," *Nat. Rev. Cancer* **21**(10), 669–680 (2021).
50. S. Xu, H. Xu, W. Wang, S. Li, H. Li, T. Li, W. Zhang, X. Yu, and L. Liu, "The role of collagen in cancer: from bench to bedside," *J. Transl. Med.* **17**(1), 309–322 (2019).
51. W. Chen, Y. Wang, N. Liu, J. Zhang, and R. Chen, "Multiphoton microscopic imaging of human normal and cancerous oesophagus tissue," *J. Microsc.* **253**(1), 79–82 (2014).
52. E. R. Baba, N. Uedo, A. L. Rodrigues, B. da Costa Martins, and F. Maluf-Filho, "Keratin pearls in magnifying endoscopy of superficial esophageal squamous cell carcinoma," *Gastrointest. Endosc.* **94**(2), 424–425 (2021).
53. R. Odze, A. Lam, A. Ochiai, and M. Washington, "Tumours of the oesophagus," *Digestive system tumours WHO classification of tumours*, 5th edn. International Agency for Research on Cancer, Lyon, 23–58 (2019).
54. C. Huang and C. Michael, "Cytomorphological features of metastatic squamous cell carcinoma in serous effusions," *Cytopathology* **25**(2), 112–119 (2014).
55. W. Zheng, Y. Wu, D. Li, and J. Y. Qu, "Autofluorescence of epithelial tissue: single-photon versus two-photon excitation," *J. Biomed. Opt.* **13**(5), 054010 (2008).
56. R. Datta, T. M. Heaster, J. T. Sharick, A. A. Gillette, and M. C. Skala, "Fluorescence lifetime imaging microscopy: fundamentals and advances in instrumentation, analysis, and applications," *J. Biomed. Opt.* **25**(07), 1–071203 (2020).
57. E. A. Shirshin, Y. I. Gurfinkel, A. V. Priezzhev, V. V. Fadeev, J. Lademann, and M. E. Darvin, "Two-photon autofluorescence lifetime imaging of human skin papillary dermis in vivo: assessment of blood capillaries and structural proteins localization," *Sci. Rep.* **7**(1), 1171 (2017).
58. E. A. Shirshin, M. V. Shirmanova, A. V. Gayer, M. M. Lukina, E. E. Nikonova, B. P. Yakimov, G. S. Budylin, V. V. Dudenkova, N. I. Ignatova, D. V. Komarov, V. V. Yakovlev, W. Becker, E. V. Zagaynova, V. I. Shcheslavskiy, and M. O. Scully, "Label-free sensing of cells with fluorescence lifetime imaging: the quest for metabolic heterogeneity," *Proc. Natl. Acad. Sci.* **119**(9), e2118241119 (2022).